Research Square

Preprints are preliminary reports that have not undergone peer review.
They should not be considered conclusive, used to inform clinical practice,
or referenced by the media as validated information.

Multisite exchange paths and zigzag antiferromagnetism in the Kitaev material RuI3 monolayer

Ke yang
University of Shanghai for Science and Technology
Zhefu Wu
Fudan University
Yaozhenghang Ma
Fudan University
Feng-Ren Fan
Soochow University
Yuxuan Zhou
Fudan University
Hua Wu
wuh@fudan.edu.cn
Fudan University

Article

Keywords:

Posted Date: November 24th, 2026

DOI: https://doi.org/10.21203/rs.3.rs-11623426/v1

License: This work is licensed under a Creative Commons Attribution 4.0 International License.
Read Full License

Additional Declarations: No competing interests reported.

Multisite exchange paths and zigzag antiferromagnetism in the Kitaev material RuI_3 monolayer

Ke Yang[1,2], Zhefu Wu[2], Yaozhenghang Ma[2], Feng-Ren Fan[2,3], Yuxuan Zhou[2], Hua Wu[2,4,5*]

[1]School of Physics, Faculty of Basic Sciences, University of Shanghai for Science and Technology, Shanghai, 200093, China.
[2*]Laboratory for Computational Physical Sciences (MOE), State Key Laboratory of Surface Physics, and Department of Physics, Fudan University, Shanghai, 200433, China.
[3]Institute for Quantum Science, School of Physical Science and Technology, Soochow University, Suzhou, 215006, China.
[4]Shanghai Qi Zhi Institute, Shanghai, 200232, China.
[5]Hefei National Laboratory, Hefei, 230088, China.

*Corresponding author(s). E-mail(s): wuh@fudan.edu.cn;

Abstract

Monolayer RuI_3, with heavy ligands, is expected to host intriguing Kitaev physics. We derive its $J_{\rm eff} = 1/2$ pseudospin model up to the third-nearest neighbors (3NN) using exact diagonalization (ED) of N-site clusters ($N = 1$–6), with crystal-field and hopping parameters from density functional theory and Wannier functions. Our results well explain the spin-orbital levels from resonant inelastic x-ray scattering experiments. We find that two-site calculations are insufficient, and multisite exchange via intermediate Ru sites is important. Therefore, we focus on six-site clusters that preserve the bond symmetry, and find that the exchange paths through one intermediate Ru site reduce the 1NN ferromagnetic Kitaev coupling but enhance the 3NN antiferromagnetic Heisenberg coupling, making the two comparable in strength. Their competition, together with sizable 1NN off-diagonal couplings, removes the Kitaev spin liquid and stabilizes zigzag antiferromagnetic order, as predicted by our 24-site ED and 72-site density-matrix renormalization group calculations.

Introduction

Quantum spin liquids (QSLs) are correlated states without conventional long-range magnetic order [1, 2]. The exactly solvable Kitaev honeycomb model [3] is a quantum compass model of the kind that Kugel and Khomskii introduced for orbital degrees of freedom [4]. Its bond-dependent interactions lead to a QSL ground state with fractionalized Majorana excitations [5, 6]. Jackeli and Khaliullin [7] proposed that the Kitaev model can be realized by $J_{\rm eff} = 1/2$ pseudospins on edge-sharing octahedra through the ligand-mediated 90° exchange paths. This proposal has stimulated extensive studies of the $5d^5$ iridate Na_2IrO_3 [8–12] and the $4d^5$ honeycomb magnet α-$RuCl_3$ [13–16]. α-$RuCl_3$ orders in the zigzag antiferromagnetic (AF) state [17] below $T_N \approx 7$ K [18], but its magnetic continuum [19–21] and the thermal Hall effect in a magnetic field [22–24] suggest proximity to the Kitaev QSL, although their origins remain debated. Kitaev physics has also been extended to the high-spin $3d^7$ Co^{2+} compounds [25, 26], such as the honeycomb cobaltate $Na_3Co_2SbO_6$ [27], the van der Waals halide CoI_2 [28] and the pyroxene $SrCoGe_2O_6$ [29].

RuI_3 was synthesized [30, 31] as the heavy-ligand analog of α-$RuCl_3$ in the RuX_3 (X = Cl, Br, I) family [32, 33], with the expectation that the heavier halogen strengthens the Kitaev coupling, which arises from the hopping through the ligand p orbitals [33, 34]. As a van der Waals material, RuI_3 may be thinned down to a monolayer, as has been achieved for α-$RuCl_3$ [35, 36], so that the Kitaev physics of RuI_3 can be examined in two dimensions. Monolayer RuI_3 is a honeycomb layer of edge-sharing RuI_6 octahedra with the Kitaev bonds X, Y and Z (Fig. 1). First-principles calculations propose different magnetic ground states, including a ferromagnetic (FM) state [37], a zigzag AF state [38], a nonmagnetic $J_{\rm eff} = 1/2$ state [39] and an octupolar AF state [40]. These different ground states indicate that the magnetism of monolayer RuI_3 is intriguing.

In many magnets, the 1NN couplings dominate, but on the honeycomb lattice the 3NN coupling is often important, whereas the 4NN coupling is usually weak [41]. With the extended I $5p$ orbitals, the 2NN and 3NN couplings may become even more important and, together with the off-diagonal couplings [42, 43], compete with the 1NN Kitaev coupling. These 2NN and 3NN couplings already grow from Cl to I in two-site calculations [32], but a two-site cluster omits the exchange paths through intermediate Ru sites. These multisite paths can modify the 1NN, 2NN and 3NN couplings. Early studies of Na_2IrO_3 found considerable delocalization of the electrons over the Ir hexagons [44, 45]. For this compound, exact diagonalization (ED) on six-site clusters gives an AF 3NN Heisenberg coupling J_3 that greatly exceeds its second-order estimate and stabilizes the zigzag order, and J_3 is about 40% of the 1NN Kitaev coupling in magnitude [46, 47]. In monolayer RuI_3, the multisite exchange paths may be even stronger and make J_3 comparable to the 1NN Kitaev coupling.

In this work, we derive the $J_{\rm eff} = 1/2$ pseudospin model of monolayer RuI_3 up to the 3NN using ED of N-site clusters (N = 1–6), with the crystal-field and hopping parameters from density functional theory (DFT) and Wannier functions. We first establish the local $J_{\rm eff} = 1/2$ ground state and compare the spin-orbital levels of Ru^{3+} with resonant inelastic x-ray scattering (RIXS) experiments [34]. We then show that two-site calculations are insufficient and focus on six-site clusters, which preserve the

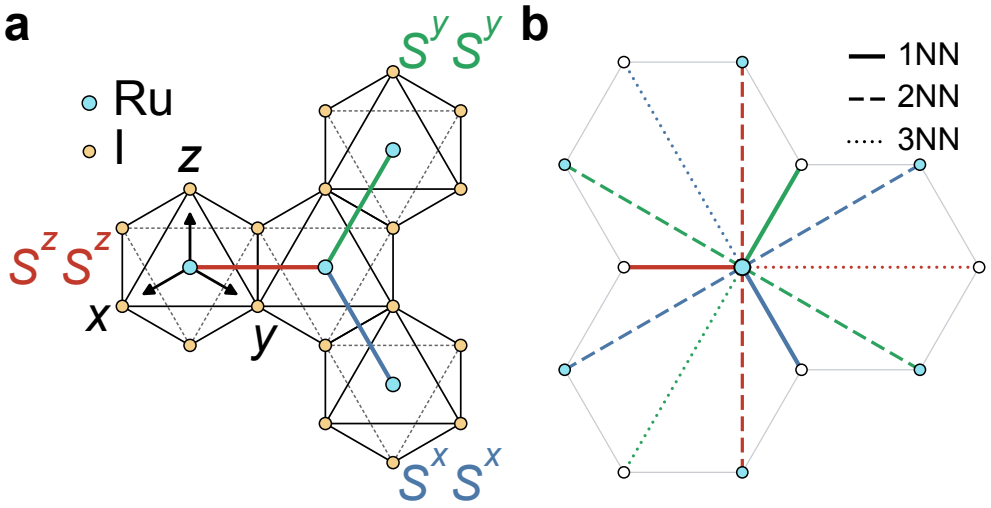

Fig. 1 Structure of monolayer RuI_3 and its Kitaev bonds. (a) Honeycomb layer of edge-sharing RuI_6 octahedra viewed along the cubic [111] axis normal to the layer, with the local cubic axes x, y and z drawn at the left Ru site. The three nearest-neighbor (1NN) bonds X, Y and Z of a Ru site (blue, green and red) carry the Kitaev couplings S^xS^x, S^yS^y and S^zS^z. (b) The 1NN (solid), second-nearest-neighbor (2NN, dashed) and third-nearest-neighbor (3NN, dotted) bonds of a Ru site, colored as the X, Y and Z bonds in (a). Filled and open circles mark the two Ru sublattices.

symmetry of the target bonds and include as many multisite exchange paths as possible. After identifying the hoppings that produce the 1NN couplings, we use a cluster expansion to determine how the multisite exchange paths of each cluster size change the 1NN, 2NN and 3NN couplings. With the six-site exchange parameters, we solve the pseudospin model by ED on a 24-site cluster and by density-matrix renormalization group (DMRG) calculations on clusters of up to 72 sites. These calculations show how the 1NN Kitaev and 3NN Heisenberg couplings compete and, together with the 1NN off-diagonal couplings, remove the Kitaev QSL and stabilize zigzag antiferromagnetic order.

Results

Local $J_{\rm eff} = 1/2$ ground state

The nonmagnetic band structure of monolayer RuI_3 from DFT within the generalized-gradient approximation (GGA) is shown in Fig. S1 of the Supplementary Information (SI). The Ru $4d$ states split into the t_{2g} triplet and the e_g doublet by $\Delta_{\rm cf} \approx 2$ eV, and both hybridize strongly with the I $5p$ states. This splitting agrees with the crystal-field parameter $10Dq = 2.05$ eV from the multiplet analysis of Ru L_3-edge RIXS [34]. We use the Hund coupling $J_H = 0.3$ eV throughout this work. This value is typical of the extended Ru $4d$ orbitals [48, 49] and consistent with the orbital-averaged value of 0.29 eV for RuI_3 from the constrained random-phase approximation [32]. The low-spin t_{2g}^5 configuration then lies $2\Delta_{\rm cf} - 6J_H \approx 2$ eV below the high-spin $t_{2g}^3e_g^2$ one (SI

Sec. II and Fig. S2). The low-spin configuration has one t_{2g} hole with $S = 1/2$ and an effective orbital angular momentum $L_{\text{eff}} = 1$.

Since the crystal field places the e_g states 2 eV above the t_{2g} states, we keep only the t_{2g} manifold and construct the single-ion Hamiltonian in its Wannier basis (SI Sec. III and Fig. S3),

$$H_{\text{one}} = H_{\text{CF}} + H_U + H_{\text{SOC}}, \tag{1}$$

where the spin-independent trigonal crystal field in the t_{2g} basis (d_{xz}, d_{yz}, d_{xy}) reads

$$H_{\text{CF}} = \begin{pmatrix} 0 & \delta & \delta \\ \delta & 0 & \delta \\ \delta & \delta & 0 \end{pmatrix}, \tag{2}$$

with $\delta_{\text{tri}} = 3|\delta|$ the splitting between the a_{1g} ($L_z = 0$) and e_g^π ($L_z = \pm 1$) orbitals. Here L_z is the component of L_{eff} along the octahedral [111] axis (SI Fig. S4). H_U is the Kanamori interaction [50] with $U = 2.0$ eV and $J_H = 0.3$ eV. This U is the same as in the DFT+U study of RuI_3 [39]. The spin-orbit coupling (SOC) term $H_{\text{SOC}} = \lambda \mathbf{L} \cdot \mathbf{S}$ has $\lambda = 0.18$ eV from the RIXS analysis [34]. The Wannier calculation gives $\delta = -14.7$ meV, a slight trigonal compression with $\delta_{\text{tri}} \approx 44$ meV (SI Sec. IV). As shown in Fig. 2a, SOC splits the t_{2g}^5 manifold into the lower $J_{\text{eff}} = 1/2$ doublet and the upper $J_{\text{eff}} = 3/2$ quartet separated by $3\lambda/2 \approx 270$ meV. The trigonal field splits the quartet into two doublets (SI Fig. S5).

For monolayer RuI_3, the ground state has a weight of 0.99 on the ideal cubic $J_{\text{eff}} = 1/2$ doublet [SI Eq. (S2)], and the Landé g factors from $\mathbf{L}+2\mathbf{S}$ are $g_c = 2.40$ out of plane and $g_{ab} = 1.79$ in plane [vertical line in Fig. 2b and its inset]. The anisotropy $g_c > g_{ab}$ is in line with the high-temperature torque measurements on RuI_3 [51]. The $J_{\text{eff}} = 1/2$ weight stays above 0.95 for $-56 < \delta < +39$ meV [Fig. 2b]. The $L_z = \pm 1$ weight exceeds 0.95 only for $\delta < -145$ meV (compression), and the $L_z = 0$ weight only for $\delta > +205$ meV (elongation) (SI Fig. S4).

As seen in Fig. 2a, the two doublets split from the $J_{\text{eff}} = 3/2$ quartet lie at 257 and 288 meV, split by 31 meV by the trigonal field. Their mean of 272 meV is in reasonable agreement with the $J_{\text{eff}} = 3/2$ spin-orbit transition observed at 300 meV by RIXS on RuI_3 [34]. In contrast, the two excited doublets would lie at 209 and 583 meV in the $L_z = \pm 1$ limit ($\delta = -145$ meV) and at 583 and 734 meV in the $L_z = 0$ limit ($\delta = +205$ meV), far from the RIXS result. Therefore, the ground state of monolayer RuI_3 is the $J_{\text{eff}} = 1/2$ state, not an $L_z = 0$ or $L_z = \pm 1$ state. The pseudospin model below is built on this state. The 31 meV splitting may be resolved by RIXS [52], infrared or Raman spectroscopy [53, 54] with higher resolution.

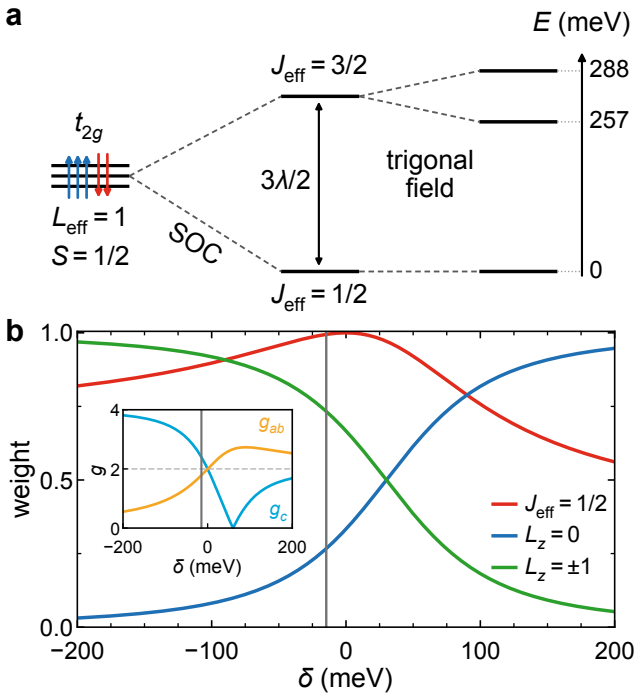

Fig. 2 Spin-orbital states of the Ru^{3+} ion in RuI_3. (a) Level scheme: spin-orbit coupling (SOC) splits the t_{2g}^5 manifold into the $J_{\rm eff} = 1/2$ doublet and the $J_{\rm eff} = 3/2$ quartet, and the trigonal field splits the quartet into two doublets. (b) Weights of the ideal $J_{\rm eff} = 1/2$ doublet (red) and of the $L_z = 0$ (blue) and $L_z = \pm 1$ (green) orbitals in the ground state versus δ of Eq. (2). The vertical line marks RuI_3. Inset: Landé g factors out of plane (g_c) and in plane (g_{ab}).

Exchange couplings up to the 3NN

The t_{2g} Wannier functions have significant weight on the I sites (SI Fig. S3). The hoppings between the Ru sites go through these I sites (SI Sec. V and Figs. S6–S7). The exchange couplings are first obtained by multiorbital ED of a two-site cluster (SI Sec. VI and Fig. S8),

$$H_{ij} = H_{\rm one}^{(i)} + H_{\rm one}^{(j)} + \sum_{\sigma} \left(\mathbf{c}_{i\sigma}^{\dagger} T_{ij}\, \mathbf{c}_{j\sigma} + \text{H.c.} \right), \tag{3}$$

with $H_{\rm one}$ of Eq. (1) on each site, $\mathbf{c}_{i\sigma}^{\dagger} = (d_{i,xz\sigma}^{\dagger}, d_{i,yz\sigma}^{\dagger}, d_{i,xy\sigma}^{\dagger})$ the t_{2g} electron creation operators of spin σ on site i, and T_{ij} the Wannier hopping matrix between the two sites. For a six-site cluster, Eq. (3) includes all six sites and the hoppings among them [46]. The six sites are chosen to preserve the symmetry of the target bond, whose couplings are extracted, and to include as many hopping paths through intermediate Ru sites as possible. The 1NN couplings are taken from the central bond of the bridge cluster, which contains a 1NN bond and the four other nearest neighbors of its two

sites (SI Fig. S9b). The 2NN and 3NN couplings are taken from the hexagon cluster of six Ru sites [Fig. 3a] (SI Sec. VII and Fig. S9c).

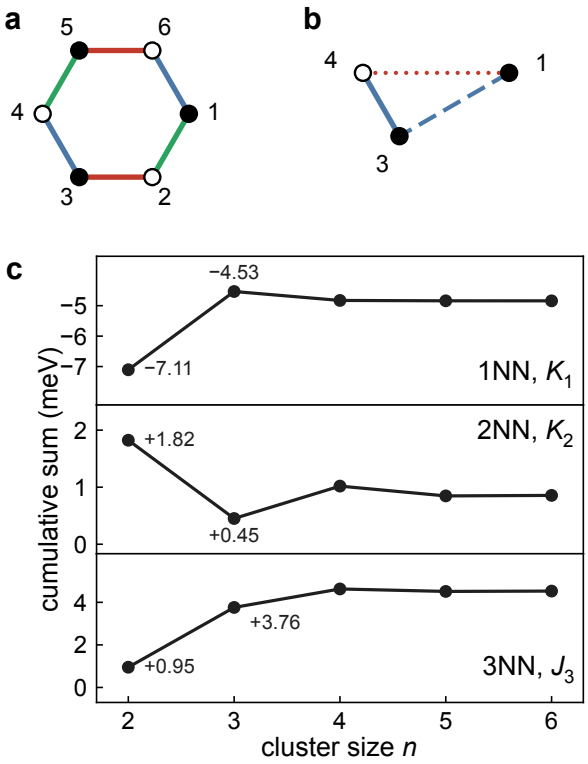

Fig. 3 Cluster expansion of the exchange couplings. (a) The six-site hexagon cluster and (b) its three-site cluster 1–3–4, with the 1NN, 2NN and 3NN bonds drawn as solid, dashed and dotted lines. (c) Cumulative sums of the cluster expansions of three representative couplings: K_1 on the central bond of the bridge cluster (SI Fig. S9b), K_2 on the 2NN bond 6–2 and J_3 on the 3NN bond 1–4. The cumulative sum at n adds up the contributions of all clusters with up to n sites, from the two-site cluster ($n = 2$) to the six-site cluster ($n = 6$).

For the 1NN and 3NN Z bonds [red in Fig. 1b], the inversion center at the midpoint makes the hopping matrix symmetric. The twofold axis along the bond makes d_{xz} and d_{yz} equivalent, so that the matrix takes the four-parameter form

$$T_Z = \begin{pmatrix} t_1 & t_2 & t_4 \\ t_2 & t_1 & t_4 \\ t_4 & t_4 & t_3 \end{pmatrix}, \tag{4}$$

where t_1–t_4 are the hopping parameters drawn in SI Figs. S6–S7. The X and Y bonds follow by the C_3 rotation about [111]. The 1NN values are $t_1 = -14.5$, $t_2 = 159.1$,

$t_3 = 91.2$ and $t_4 = -29.9$ meV, where the dominant t_2 is mediated by the bridging I ions and the direct Ru–Ru overlap t_3 is also sizable. The 3NN values are $t_1 = -13.3$, $t_2 = -19.6$, $t_3 = -28.7$ and $t_4 = 19.9$ meV. The 2NN bond has no inversion center, and its hopping matrix carries an antisymmetric part in addition,

$$T_Z^{(2)} = T_Z + \begin{pmatrix} 0 & a_1 & a_2 \\ -a_1 & 0 & -a_2 \\ -a_2 & a_2 & 0 \end{pmatrix}, \tag{5}$$

with $t_1 = -14.3$, $t_2 = -48.9$, $t_3 = -0.5$, $t_4 = 7.0$, $a_1 = 35.9$ and $a_2 = -18.1$ meV.

Projecting the lowest 2^N eigenstates of an N-site cluster onto the product states of the ideal cubic $J_{\text{eff}} = 1/2$ doublets [55] yields the bond-dependent pseudospin Hamiltonian

$$H = \sum_{n=1}^{3} \sum_{\langle ij \rangle_n} \Big[J_n \, \mathbf{S}_i \cdot \mathbf{S}_j + K_n \, S_i^\gamma S_j^\gamma + \Gamma_n \big(S_i^\alpha S_j^\beta + S_i^\beta S_j^\alpha \big) + \Gamma'_n \sum_{\mu=\alpha,\beta} \big(S_i^\gamma S_j^\mu + S_i^\mu S_j^\gamma \big) \Big] + \sum_{\langle ij \rangle_2} \mathbf{D}_{ij} \cdot \big(\mathbf{S}_i \times \mathbf{S}_j \big), \tag{6}$$

where $n = 1, 2, 3$ labels the 1NN, 2NN and 3NN bonds $\langle ij \rangle_n$ and $\{\alpha, \beta, \gamma\} = \{y, z, x\}$, $\{z, x, y\}$, $\{x, y, z\}$ for the X, Y, Z bonds. The Dzyaloshinskii–Moriya (DM) term is allowed only on the 2NN bond, which lacks the inversion center. The DM vector arises from the antisymmetric hoppings a_1 and a_2 of Eq. (5).

As seen in Table 1, going from two to six sites changes the couplings on the 1NN, 2NN and 3NN Z bonds. Even on the 1NN bond, whose two sites share two bridging I ions, K_1 is reduced by 32%, from -7.11 to -4.84 meV, whereas Γ_1 and Γ'_1 change by less than 0.15 meV (SI Table S1 and Fig. S10). On the 2NN bond, all couplings except $|\mathbf{D}|$ are reduced by more than a factor of two. The largest change appears on the 3NN bond, where J_3 increases by a factor of 4.8, from 0.95 to 4.53 meV. Therefore, the two-site cluster does not give reliable couplings for RuI_3, and all subsequent pseudospin calculations use the six-site values. The extraction is also checked against published couplings of α-$RuCl_3$ (SI Table S2). For the six-site couplings, varying U, J_H and λ gives $J_3/|K_1|$ between 0.79 and 1.33 (SI Sec. VIII and Table S3), so J_3 stays comparable to the 1NN Kitaev coupling. The origin of these differences is analyzed in the next subsection.

Table 1 Exchange parameters (meV) of monolayer RuI_3 on the 1NN, 2NN and 3NN Z bonds from the two- and six-site clusters.

		J	K	Γ	Γ'	$\lvert\mathbf{D}\rvert$
1NN	two-site	−1.62	−7.11	−3.98	−3.47	0
	six-site	−1.43	−4.84	−3.95	−3.33	0
2NN	two-site	−1.58	1.82	1.17	1.81	1.42
	six-site	−0.62	0.86	0.51	0.80	1.34
3NN	two-site	0.95	0.00	0.01	−0.18	0
	six-site	4.53	0.09	−0.06	−0.29	0

Origin of the exchange couplings

To find which hoppings produce the four 1NN couplings, we start the two-site ED with only t_2 of the four 1NN hoppings t_1–t_4 in Eq. (4), then add t_1 and t_3, and finally add t_4 together with the trigonal crystal field δ (SI Fig. S7). The hopping t_2 through the two bridging I ions alone gives a pure Kitaev coupling $K = -9.22$ meV. The Heisenberg term vanishes because the paths through the two I ions interfere destructively [7, 42]. Adding the direct Ru–Ru overlaps t_1 and t_3 changes K to -7.57 meV and generates $\Gamma = -3.44$ meV, whereas $J = 0.03$ meV is negligible and Γ' remains zero. In second-order perturbation theory, Γ is proportional to $t_2(t_1 - t_3)$ [42], and it is large in RuI_3 because $t_3 = 91.2$ meV is much larger in magnitude than $t_1 = -14.5$ meV. For t_3, the d_{xy} lobes point along the Ru–Ru bond and overlap head-on. For t_1, the d_{xz} and d_{yz} lobes overlap only sideways. Therefore, Γ arises mainly from the direct Ru–Ru overlap t_3. The trigonal distortion gives rise to the hopping t_4 and the crystal field δ. Adding both generates $\Gamma' = -3.47$ meV and an FM $J = -1.62$ meV and yields the two-site values of Table 1. Hence, Γ' and the FM J arise from the trigonal distortion. A pure Kitaev bond needs a strong t_2, weak direct overlaps and no trigonal distortion, whereas RuI_3 has a sizable t_3 and a finite distortion.

We now turn to the exchange paths through intermediate Ru sites, which the two-site cluster does not contain. To include them, we perform ED on all possible three- to six-site clusters that contain the target bond (SI Figs. S11–S13). For the 3NN bond 1–4 of the hexagon [Fig. 3a], the two-site cluster gives $J_3 = 0.95$ meV. The shortest additional exchange path involves one intermediate Ru site, as in the three-site cluster 1–3–4 [Fig. 3b]. In this cluster, site 3 is a 2NN of site 1 and a 1NN of site 4. In the lowest-order process, an electron hops from site 1 to site 3 by the 2NN hopping, then from site 3 to site 4 by the 1NN hopping, and returns to site 1 by the 3NN hopping, going once around the triangle 1–3–4. This process needs the 1NN, 2NN and 3NN hoppings together, whereas the two-site cluster contains only the direct 3NN hopping between sites 1 and 4. Besides 1–3–4, the bond 1–4 belongs to three equivalent triangles, 1–2–4, 1–4–5 and 1–4–6, and each of the four triangles adds 0.70 meV to J_3. The two-site value and the four triangles thus give $J_3 = 3.76$ meV. The four- to six-site clusters add the remaining 0.77 meV, bringing J_3 to 4.53 meV [Fig. 3c]. To test the role of these triangle processes, we set the 1NN, 2NN or 3NN hopping matrix to zero in the six-site ED. In each case, J_3 drops to 0.93–0.97 meV, close to the two-site value (SI

Table S1 and Fig. S10). The weak direct 3NN hopping alone gives only a small J_3. Paths through an intermediate Ru site combine it with the strong 1NN hopping and the 2NN hopping, producing most of the enhancement.

The multisite exchange paths also change the 1NN couplings. For the 1NN bond, the shortest paths again run through one intermediate site. For the central 1NN bond 1–2 of the bridge cluster (SI Fig. S9b), the two-site cluster gives an FM $K_1 = -7.11$ meV. Each of the other four sites forms a triangle with sites 1 and 2, giving the three-site clusters 1–2–3, 1–2–4, 1–2–5 and 1–2–6 (SI Fig. S11b). These triangles contain two 1NN bonds and one 2NN bond, so they combine only the 1NN and 2NN hoppings. Each triangle adds an AF Kitaev contribution of +0.64 meV, which reduces the magnitude of the FM K_1, so the two-site value and the four triangles give $K_1 = -4.53$ meV. The four- to six-site clusters slightly increase its magnitude again to -4.84 meV (SI Fig. S11). To isolate the role of the 2NN hopping, we repeat the six-site ED with only the 1NN hoppings and obtain $K_1 = -5.89$ meV. Adding the 2NN hopping that closes the triangles gives $K_1 = -4.85$ meV (SI Table S1).

The 2NN couplings are changed in the same way. For the 2NN bond 6–2 of the hexagon [Fig. 3a], the two-site cluster gives an AF $K_2 = 1.82$ meV. Among the four triangles that contain this bond, the triangle 1–2–6 dominates. In this triangle, site 1 is the common 1NN of sites 2 and 6, and the triangle gives -1.38 meV to K_2. The other three triangles nearly cancel each other, so the three-site clusters bring K_2 to 0.45 meV, and the four- to six-site clusters partly restore it to 0.86 meV (SI Fig. S12). Therefore, the multisite exchange paths reduce the AF K_2 by more than a factor of two.

Figure 3c shows that the leading corrections to J_3 and K_1 arise from three-site triangles containing one intermediate Ru site. Including contributions from clusters of up to four sites reproduces both six-site couplings to within 2%. By combining different hopping channels, these multisite paths enhance the AF J_3 and weaken the FM K_1, bringing the 3NN Heisenberg exchange to the scale of the 1NN Kitaev coupling. The sizable 1NN off-diagonal couplings have a different microscopic origin: direct Ru–Ru overlap and trigonal distortion. They are already present in the two-site model and remain largely unchanged by the multisite corrections. RuI_3 therefore has competing Kitaev, off-diagonal and 3NN Heisenberg couplings of comparable strength, whose balance determines its magnetic ground state.

Magnetic ground state and phase diagram

To determine the magnetic order selected by these competing exchanges, we solve the pseudospin Hamiltonian of Eq. (6) by ED on the 24-site periodic cluster, using the six-site couplings of Table 1 (SI Fig. S9d). We first isolate the role of the 1NN couplings and vary the ratio of J and K through $J = A\cos\varphi$ and $K = A\sin\varphi$, with $A = (J^2+K^2)^{1/2}$ (Fig. 4). The phase boundaries are the peaks of $-d^2E_{\mathrm{GS}}/d\varphi^2$, where E_{GS} is the ground-state energy, and the order in each φ window is identified from the static spin structure factor $S(\mathbf{q})$ (SI Figs. S14–S16).

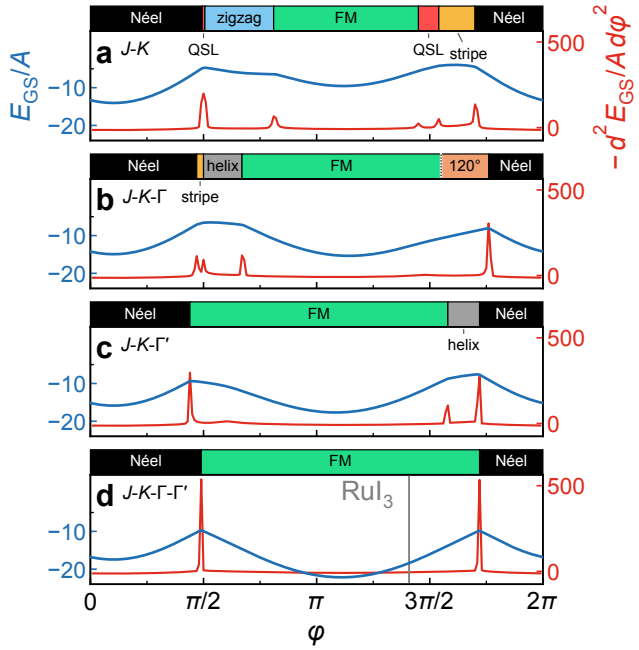

Fig. 4 ED phase diagrams of the pseudospin Hamiltonian with only the 1NN couplings on the 24-site cluster, with $J = A\cos\varphi$ and $K = A\sin\varphi$: (a) J-K, (b) J-K-Γ, (c) J-K-Γ', and (d) J-K-Γ-Γ', where $\Gamma/A = -0.78$ and $\Gamma'/A = -0.66$ are the six-site values of RuI_3. Blue: ground-state energy E_{GS}/A; red: $-A^{-1}d^2E_{GS}/d\varphi^2$, whose peaks mark the phase boundaries. The colored bar above each panel labels the phases (SI Sec. IX), and the gray line in (d) marks RuI_3 ($\varphi \approx 1.41\pi$).

The J-K model [Fig. 4a] reproduces the known sequence of Néel, zigzag, FM and stripe orders interrupted by the Kitaev QSL windows around $\varphi = \pi/2$ and $3\pi/2$ [8, 11]. With the six-site values $J = -1.43$ and $K = -4.84$ meV, the RuI_3 point lies in the FM phase at $\varphi \approx 1.41\pi$. Adding Γ or Γ' at its RuI_3 value removes both QSL windows [Figs. 4b and 4c]. With both present, only the Néel and FM phases survive [Fig. 4d]. The resulting 1NN model still places RuI_3 in the FM phase.

To test the stability of this FM state against longer-range exchange, we add the six-site 2NN and 3NN couplings (Fig. 5). The 2NN couplings only narrow the FM window [Fig. 5a]. In contrast, the 3NN couplings suppress the FM phase throughout the scan, leaving Néel and zigzag regions [Figs. 5b and 5c]. This change is driven mainly by the large AF J_3. At the RuI_3 point ($\varphi \approx 1.41\pi$), zigzag correlations dominate near the boundary with the Néel region [Fig. 5c].

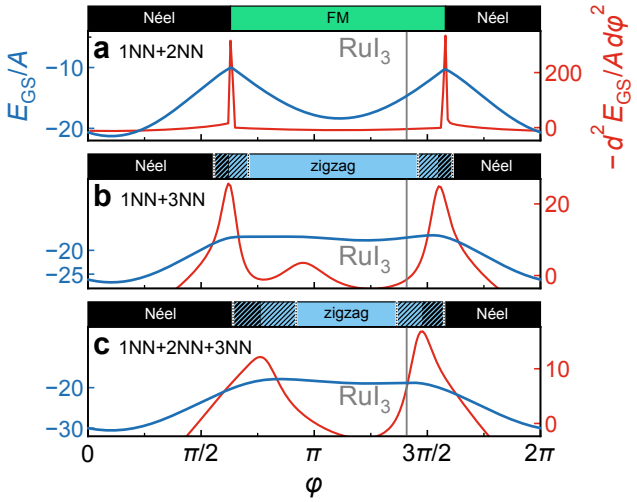

Fig. 5 ED phase diagrams of the pseudospin Hamiltonian of Fig. 4d with the 2NN and 3NN couplings of RuI_3 added: (a) 1NN+2NN, (b) 1NN+3NN, and (c) 1NN+2NN+3NN. Blue and red as in Fig. 4. Hatched: the Néel–zigzag crossover regions, where the finite-cluster spin correlations show both Néel and zigzag character (SI Sec. IX). The gray line marks RuI_3.

The competition between Néel and zigzag can be understood from their classical energies. Both states gain the same energy from J_3, but zigzag keeps two of the three 1NN bonds ferromagnetic and gains more energy from the FM 1NN couplings. For the full RuI_3 couplings, zigzag lies 0.58 meV per site below Néel (SI Sec. XI). It also remains the lowest of the four collinear states, FM, Néel, zigzag and stripe, for all parameter sets of SI Table S3.

Despite this classical preference, the 24-site quantum ground state retains both zigzag and Néel correlations near the boundary. Fitting these finite-cluster correlations gives weights of 79% zigzag and 21% Néel (SI Sec. IX). Its $S(\mathbf{q})$ likewise shows zigzag peaks at the M points together with Néel peaks [Fig. 6c]. RuI_3 thus lies in the hatched crossover region of Fig. 5c. To determine which order persists, we follow both correlations with cluster size.

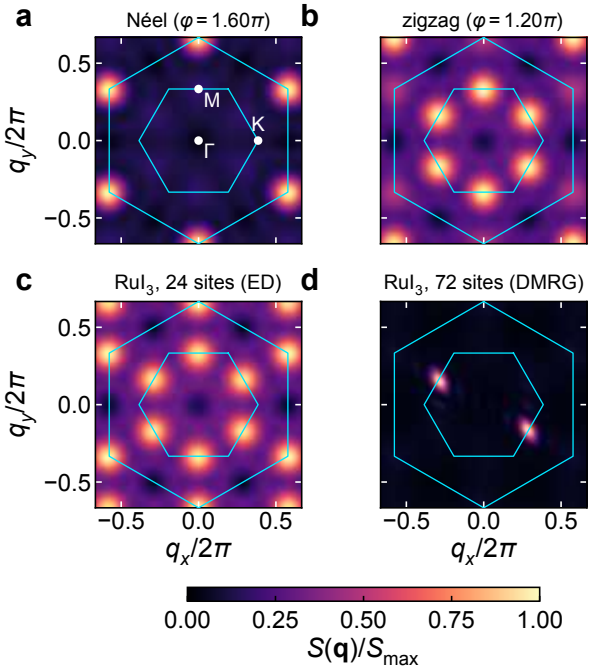

Fig. 6 Static spin structure factor $S(\mathbf{q})/S_{\max}$ of the pseudospin Hamiltonian with the 1NN, 2NN and 3NN couplings. (a)–(c) ED on the 24-site cluster for the Néel state and the zigzag state of Fig. 5c and for RuI_3. (d) DMRG on the 72-site cluster for RuI_3. Cyan lines mark the first and second Brillouin zones, and Γ, M and K in (a) mark the center, the edge midpoint and the corner of the first zone.

DMRG agrees with ED on the 24-site cluster and allows us to follow the correlations up to 72 sites (SI Figs. S17–S19 and Table S4). The Néel correlations weaken as the system grows. The squared Néel order parameter decreases from 0.097 to 0.019, whereas the squared zigzag order parameter summed over the three equivalent orientations remains sizable at 0.25–0.29. Tests with weak pinning fields on smaller clusters also show a weakening Néel response with increasing size, whereas the zigzag response approaches saturation (SI Sec. X and Table S5). On the 72-site cluster, the DMRG state selects a single zigzag domain (SI Fig. S18), whose peaks dominate $S(\mathbf{q})$ [Fig. 6d]. These results support a zigzag ground state for RuI_3.

In this 72-site zigzag state, the local pseudospin has an average length of 0.455 and is tilted by 16° from the c axis toward the zigzag chain. The anisotropic g factors, $g_c = 2.40$ and $g_{ab} = 1.79$, give an ordered moment of approximately $1.1\,\mu_B$, tilted by 12° from the c axis.

The selected zigzag state is also stable in linear spin-wave theory, with a magnon gap of 6.7 meV, whereas the Néel state is unstable near the M points (SI Fig. S20). The gap reflects the exchange anisotropy, which permits finite-temperature order that would be forbidden in the isotropic two-dimensional model [56]. To estimate the ordering temperature, we perform classical Monte Carlo (MC) simulations of the same Hamiltonian (SI Sec. XII and Figs. S21–S22). These give zigzag order below

$T_N \approx 12$ K, whereas the model with only 1NN couplings orders ferromagnetically below $T_c \approx 18$ K. The pseudospin tilt of 17.7° from the c axis is close to the 16° obtained by DMRG.

Discussion

Reaching the Kitaev limit in RuI_3 would require suppressing both the 3NN Heisenberg coupling and the 1NN off-diagonal couplings. A weaker trigonal distortion reduces Γ' and the FM 1NN Heisenberg coupling. Our results also suggest that less extended ligand p and metal d orbitals help to approach the Kitaev QSL. A lighter ligand reduces the 2NN and 3NN hoppings, and less extended metal d orbitals reduce the direct overlaps that generate Γ. In $3d$ transition-metal oxides with O $2p$ ligands, the compact orbitals on both ions would suppress both effects. However, unlike a $4d^5$ ion in the low-spin t_{2g}^5 state, a $3d^5$ ion usually takes the high-spin state because of its strong Hund coupling. Even if a strong crystal field made it low-spin, its weak SOC would not stabilize a robust $J_{\text{eff}} = 1/2$ doublet. Among the $3d$ ions, the high-spin d^7 Co^{2+} ion would be the alternative, because its ground state could be a spin-orbit-entangled pseudospin-1/2 doublet with bond-dependent exchange [25, 26].

In summary, we have studied monolayer RuI_3, a Kitaev spin-liquid candidate that was expected to have a stronger Kitaev coupling than α-$RuCl_3$ owing to the heavier I ligand. Our calculations confirm the local $J_{\text{eff}} = 1/2$ ground state and well explain the spin-orbital levels observed by RIXS. We find that two-site calculations are insufficient, and the multisite exchange paths through intermediate Ru sites are important. In the six-site clusters, these paths, mainly those through one intermediate Ru site, reduce the 1NN FM Kitaev coupling but enhance the 3NN AF Heisenberg coupling J_3, making the two comparable in strength. The 1NN off-diagonal couplings, already present in the two-site calculations, are also comparable in magnitude to the 1NN Kitaev coupling. Therefore, the heavy ligand does not bring RuI_3 to the Kitaev limit. With only the 1NN couplings, the pseudospin Hamiltonian has an FM ground state. In strong contrast, our 24-site ED and 72-site DMRG calculations of the Hamiltonian with couplings up to the 3NN predict zigzag AF order. The competition between the 1NN Kitaev and 3NN Heisenberg couplings, together with the 1NN off-diagonal couplings, removes the Kitaev QSL and stabilizes this order. The predicted ordered moment of $1.1\,\mu_B$ tilted by 12° from the c axis, the magnon gap of 6.7 meV given by spin-wave calculations, and the anisotropic Landé g factors $g_c = 2.40$ and $g_{ab} = 1.79$ given by single-ion calculations are all worth an experimental study.

This work is dedicated to the memory of Daniel I. Khomskii. The bond-dependent exchange of Kitaev materials is a magnetic realization of the compass model that he introduced with Kugel for orbital degrees of freedom [4], and the analysis of the hopping channels and exchange paths in this work follows his way of thinking about the orbital physics of transition-metal compounds. H.W. is grateful for the years of collaboration and friendship with him, and K.Y. for the discussions with him and the work they published together.

Methods

First-principles calculations

DFT calculations are performed for the honeycomb RuI_3 monolayer in the $P\bar{3}1m$ structure with a 15 Å out-of-plane cell length, using the projector augmented-wave method [57] in VASP [58, 59] with the Perdew–Burke–Ernzerhof GGA functional [60], a 500 eV plane-wave cutoff and a 10^{-6} eV electronic convergence threshold. The cell shape and the internal coordinates are relaxed on a $7 \times 7 \times 1$ k-mesh in a spin-polarized calculation started from an FM configuration until the forces fall below 0.01 eV Å^{-1}. The relaxed lattice constants are $a = b = 7.01$ Å. From the nonmagnetic band structure without SOC on a $12\times12\times1$ k-mesh, the six t_{2g} bands are disentangled from the neighboring bands within an energy window from -0.9 to $+0.7$ eV relative to the Fermi level and projected onto the Ru t_{2g} orbitals with WANNIER90 [61]. No spread minimization is applied, so that each Wannier function keeps its t_{2g} symmetry (SI Sec. III).

Electronic model and exchange couplings

The electronic model keeps only the Ru t_{2g} orbitals with an effective on-site SOC. We assume the Mott-insulating limit, with a localized $J_{\text{eff}} = 1/2$ moment on each Ru. DFT+U predicts an insulating monolayer [39], whereas DFT combined with dynamical mean-field theory places it near the metal–insulator boundary and suggests that it may remain metallic [62]. The multiorbital Hubbard model with the Kanamori interaction [49, 50] is solved by ED with $U = 2.0$ eV, $J_H = 0.3$ eV and $\lambda = 0.18$ eV. The exchange couplings are obtained by projecting the lowest eigenstates of the two-site cluster and of the six-site bridge and hexagon clusters [46] onto the product states of the ideal cubic $J_{\text{eff}} = 1/2$ doublets (SI Secs. VI and VII). The projected low-energy states are Löwdin-orthonormalized, and the bilinear couplings are read from the projected Hamiltonian. The terms beyond the bilinear couplings have a root-mean-square size of 0.05 meV on the bridge and 0.09 meV on the hexagon. In the cluster expansion, every subcluster that contains the target bond is diagonalized and projected in the same way. Each subcluster is assigned the part of the coupling that first appears on it. This part is called the cumulant and equals the coupling of the subcluster minus the cumulants of all its smaller subclusters that contain this bond. The cumulants of the 16 subclusters add up to the six-site value.

Pseudospin-model solvers

The pseudospin Hamiltonian is solved by ED on the 24-site periodic cluster of SI Fig. S9, by DMRG [63] with ITensors [64] on the periodic clusters of 24 to 72 sites of SI Fig. S17, and by classical MC simulations. The ED uses the Lanczos algorithm with a Krylov dimension of 20 and a residual below 10^{-10}. The results are checked against random restarts. The DMRG uses the two-site algorithm with a discarded-weight cutoff of 10^{-10}. The bond dimension reaches 2000 on 24 and 32 sites, 1500 on 48 sites and 1000 on 72 sites (SI Sec. X). The truncation errors of 1×10^{-5} to 4×10^{-4} are listed in SI Table S4. On 24 sites, the DMRG reproduces the ED energies within 0.25%

(SI Fig. S19). The response to a pinning field is obtained by adding $-h\sum_i \epsilon_i^P\,\mathbf{n}_P\cdot\mathbf{S}_i$ to the DMRG Hamiltonian, with $\epsilon_i^P=\pm1$ the signs of the pattern P, $\mathbf{n}_P$ its easy axis and $h\le 0.2$ meV. Linear spin-wave theory is applied to the Néel and zigzag states on their two- and four-site magnetic cells (SI Sec. XI). In the MC simulations, the pseudospins are classical vectors of length 1/2 on periodic lattices of 8×8 to 24×24 unit cells. They are updated by the Metropolis method with overrelaxation, and the ordering temperature is taken from the specific-heat peak (SI Sec. XII).

Data availability. The data that support the findings of this study are available from the corresponding author upon reasonable request.

Code availability. The codes used in this study are available from the corresponding author upon reasonable request.

Acknowledgements. This work was supported by the National Natural Science Foundation of China (Grants No. 12574127, No. 12674133, No. 12241402, and No. 12504217) and by the Quantum Science and Technology–National Science and Technology Major Project (Grant No. 2024ZD0300102). F.-R.F. was also supported by the Open Research Fund of the State Key Laboratory of Surface Physics, Fudan University (Grant No. KF2025_04).

Author contributions. H.W. and K.Y. conceived and supervised the project. K.Y. performed the exact-diagonalization, DMRG and spin-wave calculations and analyzed the data. Z.W. and Y.M. performed the DFT, Wannier and Monte Carlo calculations. F.-R.F. and Y.Z. contributed to the analysis and discussion of the results. H.W. and K.Y. wrote the manuscript. All authors discussed the results and commented on the manuscript.

Competing interests. All authors declare no financial or non-financial competing interests.

References

[1] Anderson, P. W. Resonating valence bonds: a new kind of insulator? *Mater. Res. Bull.* **8**, 153–160 (1973).

[2] Balents, L. Spin liquids in frustrated magnets. *Nature* **464**, 199–208 (2010).

[3] Kitaev, A. Anyons in an exactly solved model and beyond. *Ann. Phys.* **321**, 2–111 (2006).

[4] Kugel', K. I. & Khomskii, D. I. The Jahn–Teller effect and magnetism: transition metal compounds. *Sov. Phys. Usp.* **25**, 231–256 (1982).

[5] Takagi, H., Takayama, T., Jackeli, G., Khaliullin, G. & Nagler, S. E. Concept and realization of Kitaev quantum spin liquids. *Nat. Rev. Phys.* **1**, 264–280 (2019).

[6] Trebst, S. & Hickey, C. Kitaev materials. *Phys. Rep.* **950**, 1–37 (2022).

[7] Jackeli, G. & Khaliullin, G. Mott insulators in the strong spin-orbit coupling limit: from Heisenberg to a quantum compass and Kitaev models. *Phys. Rev. Lett.* **102**, 017205 (2009).

[8] Chaloupka, J., Jackeli, G. & Khaliullin, G. Kitaev-Heisenberg model on a honeycomb lattice: possible exotic phases in iridium oxides A_2IrO_3. *Phys. Rev. Lett.* **105**, 027204 (2010).

[9] Liu, X. *et al.* Long-range magnetic ordering in Na_2IrO_3. *Phys. Rev. B* **83**, 220403 (2011).

[10] Ye, F. *et al.* Direct evidence of a zigzag spin-chain structure in the honeycomb lattice: a neutron and x-ray diffraction investigation of single-crystal Na_2IrO_3. *Phys. Rev. B* **85**, 180403 (2012).

[11] Chaloupka, J., Jackeli, G. & Khaliullin, G. Zigzag magnetic order in the iridium oxide Na_2IrO_3. *Phys. Rev. Lett.* **110**, 097204 (2013).

[12] Chun, S. H. *et al.* Direct evidence for dominant bond-directional interactions in a honeycomb lattice iridate Na_2IrO_3. *Nat. Phys.* **11**, 462–466 (2015).

[13] Plumb, K. W. *et al.* α-$RuCl_3$: a spin-orbit assisted Mott insulator on a honeycomb lattice. *Phys. Rev. B* **90**, 041112 (2014).

[14] Sandilands, L. J., Tian, Y., Plumb, K. W., Kim, Y.-J. & Burch, K. S. Scattering continuum and possible fractionalized excitations in α-$RuCl_3$. *Phys. Rev. Lett.* **114**, 147201 (2015).

[15] Kim, H.-S., V., V. S., Catuneanu, A. & Kee, H.-Y. Kitaev magnetism in honeycomb $RuCl_3$ with intermediate spin-orbit coupling. *Phys. Rev. B* **91**, 241110 (2015).

[16] Banerjee, A. *et al.* Proximate Kitaev quantum spin liquid behaviour in a honeycomb magnet. *Nat. Mater.* **15**, 733–740 (2016).

[17] Johnson, R. D. *et al.* Monoclinic crystal structure of α-$RuCl_3$ and the zigzag antiferromagnetic ground state. *Phys. Rev. B* **92**, 235119 (2015).

[18] Cao, H. B. *et al.* Low-temperature crystal and magnetic structure of α-$RuCl_3$. *Phys. Rev. B* **93**, 134423 (2016).

[19] Banerjee, A. *et al.* Neutron scattering in the proximate quantum spin liquid α-$RuCl_3$. *Science* **356**, 1055–1059 (2017).

[20] Winter, S. M. *et al.* Breakdown of magnons in a strongly spin-orbital coupled magnet. *Nat. Commun.* **8**, 1152 (2017).

[21] Winter, S. M., Riedl, K., Kaib, D., Coldea, R. & Valentí, R. Probing α-$RuCl_3$ beyond magnetic order: effects of temperature and magnetic field. *Phys. Rev. Lett.* **120**, 077203 (2018).

[22] Kasahara, Y. *et al.* Majorana quantization and half-integer thermal quantum Hall effect in a Kitaev spin liquid. *Nature* **559**, 227–231 (2018).

[23] Yokoi, T. *et al.* Half-integer quantized anomalous thermal Hall effect in the Kitaev material candidate α-$RuCl_3$. *Science* **373**, 568–572 (2021).

[24] Czajka, P. *et al.* Planar thermal Hall effect of topological bosons in the Kitaev magnet α-$RuCl_3$. *Nat. Mater.* **22**, 36–41 (2023).

[25] Liu, H. & Khaliullin, G. Pseudospin exchange interactions in d^7 cobalt compounds: possible realization of the Kitaev model. *Phys. Rev. B* **97**, 014407 (2018).

[26] Sano, R., Kato, Y. & Motome, Y. Kitaev-Heisenberg Hamiltonian for high-spin d^7 Mott insulators. *Phys. Rev. B* **97**, 014408 (2018).

[27] Liu, H., Chaloupka, J. & Khaliullin, G. Kitaev spin liquid in 3d transition metal compounds. *Phys. Rev. Lett.* **125**, 047201 (2020).

[28] Ma, Y., Yang, K., Zhou, Y. & Wu, H. Kitaev interaction and possible spin liquid state in CoI_2 and $Co_{2/3}Mg_{1/3}I_2$. *Phys. Rev. B* **112**, L220412 (2025).

[29] Maksimov, P. A. *et al.* Cobalt-based pyroxenes: a new playground for Kitaev physics. *Proc. Natl Acad. Sci. USA* **121**, e2409154121 (2024).

[30] Nawa, K. *et al.* Strongly electron-correlated semimetal RuI_3 with a layered honeycomb structure. *J. Phys. Soc. Jpn.* **90**, 123703 (2021).

[31] Ni, D., Gui, X., Powderly, K. M. & Cava, R. J. Honeycomb-structure RuI_3, a new quantum material related to α-$RuCl_3$. *Adv. Mater.* **34**, 2106831 (2022).

[32] Kaib, D. A. S. *et al.* Electronic and magnetic properties of the RuX_3 (X = Cl, Br, I) family: two siblings—and a cousin? *npj Quantum Mater.* **7**, 75 (2022).

[33] Imai, Y. *et al.* Zigzag magnetic order in the Kitaev spin-liquid candidate material $RuBr_3$ with a honeycomb lattice. *Phys. Rev. B* **105**, L041112 (2022).

[34] Gretarsson, H. *et al.* $J = 1/2$ pseudospins and d-p hybridization in the Kitaev spin liquid candidates RuX_3 (X = Cl, Br, I). *Phys. Rev. B* **109**, L180413 (2024).

[35] Weber, D. *et al.* Magnetic properties of restacked 2D spin 1/2 honeycomb $RuCl_3$ nanosheets. *Nano Lett.* **16**, 3578–3584 (2016).

[36] Yang, B. *et al.* Magnetic anisotropy reversal driven by structural symmetry-breaking in monolayer α-$RuCl_3$. *Nat. Mater.* **22**, 50–57 (2023).

[37] Huang, C. *et al.* Quantum anomalous Hall effect in ferromagnetic transition metal halides. *Phys. Rev. B* **95**, 045113 (2017).

[38] Ersan, F. *et al.* Exploring the electronic and magnetic properties of new metal halides from bulk to two-dimensional monolayer: RuX_3 (X = Br, I). *J. Magn. Magn. Mater.* **476**, 111–119 (2019).

[39] Liu, L. *et al.* Contrasting electronic states of RuI_3 and $RuCl_3$. *Phys. Rev. B* **107**, 165134 (2023).

[40] Qiu, W.-X. *et al.* Efficient method for prediction of metastable or ground multipolar ordered states and its application in monolayer α-RuX_3 (X = Cl, I). *Phys. Rev. Lett.* **127**, 147202 (2021).

[41] Yang, K. *et al.* Understanding the Ising zigzag antiferromagnetism of $FePS_3$ and $FePSe_3$ monolayers. *Phys. Rev. B* **110**, 024427 (2024).

[42] Rau, J. G., Lee, E. K.-H. & Kee, H.-Y. Generic spin model for the honeycomb iridates beyond the Kitaev limit. *Phys. Rev. Lett.* **112**, 077204 (2014).

[43] Rau, J. G. & Kee, H.-Y. Trigonal distortion in the honeycomb iridates: proximity of zigzag and spiral phases in Na_2IrO_3. Preprint at https://arxiv.org/abs/1408.4811 (2014).

[44] Mazin, I. I., Jeschke, H. O., Foyevtsova, K., Valentí, R. & Khomskii, D. I. Na_2IrO_3 as a molecular orbital crystal. *Phys. Rev. Lett.* **109**, 197201 (2012).

[45] Foyevtsova, K., Jeschke, H. O., Mazin, I. I., Khomskii, D. I. & Valentí, R. Ab initio analysis of the tight-binding parameters and magnetic interactions in Na_2IrO_3. *Phys. Rev. B* **88**, 035107 (2013).

[46] Winter, S. M., Li, Y., Jeschke, H. O. & Valentí, R. Challenges in design of Kitaev materials: magnetic interactions from competing energy scales. *Phys. Rev. B* **93**, 214431 (2016).

[47] Winter, S. M. *et al.* Models and materials for generalized Kitaev magnetism. *J. Phys. Condens. Matter* **29**, 493002 (2017).

[48] Khomskii, D. I. *Transition Metal Compounds* (Cambridge Univ. Press, 2014).

[49] Georges, A., de' Medici, L. & Mravlje, J. Strong correlations from Hund's coupling. *Annu. Rev. Condens. Matter Phys.* **4**, 137–178 (2013).

[50] Kanamori, J. Electron correlation and ferromagnetism of transition metals. *Prog. Theor. Phys.* **30**, 275–289 (1963).

[51] Ma, Z. *et al.* Anisotropic magnetic interactions in a candidate Kitaev spin liquid close to a metal-insulator transition. *Commun. Phys.* **7**, 390 (2024).

[52] Lebert, B. W. *et al.* Resonant inelastic x-ray scattering study of α-$RuCl_3$: a progress report. *J. Phys. Condens. Matter* **32**, 144001 (2020).

[53] Sandilands, L. J. *et al.* Spin-orbit excitations and electronic structure of the putative Kitaev magnet α-$RuCl_3$. *Phys. Rev. B* **93**, 075144 (2016).

[54] Warzanowski, P. *et al.* Multiple spin-orbit excitons and the electronic structure of α-$RuCl_3$. *Phys. Rev. Res.* **2**, 042007 (2020).

[55] Riedl, K., Li, Y., Valentí, R. & Winter, S. M. Ab initio approaches for low-energy spin Hamiltonians. *Phys. Status Solidi B* **256**, 1800684 (2019).

[56] Mermin, N. D. & Wagner, H. Absence of ferromagnetism or antiferromagnetism in one- or two-dimensional isotropic Heisenberg models. *Phys. Rev. Lett.* **17**, 1133–1136 (1966).

[57] Blöchl, P. E. Projector augmented-wave method. *Phys. Rev. B* **50**, 17953–17979 (1994).

[58] Kresse, G. & Hafner, J. Ab initio molecular dynamics for liquid metals. *Phys. Rev. B* **47**, 558–561 (1993).

[59] Kresse, G. & Furthmüller, J. Efficient iterative schemes for ab initio total-energy calculations using a plane-wave basis set. *Phys. Rev. B* **54**, 11169–11186 (1996).

[60] Perdew, J. P., Burke, K. & Ernzerhof, M. Generalized gradient approximation made simple. *Phys. Rev. Lett.* **77**, 3865–3868 (1996).

[61] Mostofi, A. A. *et al.* wannier90: a tool for obtaining maximally-localised Wannier functions. *Comput. Phys. Commun.* **178**, 685–699 (2008).

[62] Samanta, S., Hong, D. & Kim, H.-S. Electronic structures of Kitaev magnet candidates $RuCl_3$ and RuI_3. *Nanomaterials* **14**, 9 (2024).

[63] White, S. R. Density matrix formulation for quantum renormalization groups. *Phys. Rev. Lett.* **69**, 2863–2866 (1992).

[64] Fishman, M., White, S. R. & Stoudenmire, E. M. The ITensor software library for tensor network calculations. *SciPost Phys. Codebases* 4 (2022).

Supplementary Files

This is a list of supplementary files associated with this preprint. Click to download.

- SupplementaryInformationRuI3.pdf